Vibration and sound radiation of an acoustic black hole plate immersed in heavy fluid

Li Ma[1] and Li Cheng[2,a] (iD)

[1]*School of Naval Architecture, Ocean and Energy Power Engineering, Wuhan University of Technology, Wuhan, China*

[2]*Department of Mechanical Engineering, The Hong Kong Polytechnic University, Hong Kong*

ABSTRACT:

Vibrational acoustic black holes (ABHs) have shown great promise for reducing structural vibrations and sound radiation in light fluids. However, it is still unknown whether the acoustic black hole (ABH) effect can be materialized in heavy fluids. This paper discusses this issue by developing a semi-analytical model on a simply supported ABH plate that vibrates and radiates sound into water. The proposed model is validated by finite element models and used to investigate the vibration and sound radiation properties of the ABH plate in different frequency ranges. The results show that the ABH effect can be systematically manifested in heavy fluids, as reflected by a significant increase in structural damping and a decrease in vibration and sound radiation. Numerical analysis of the radiation damping and mass loading effects shows that the radiation damping has little effect on the vibration reduction of the water-loaded plate. However, the mass loading effect mitigates the low-frequency drawback of conventional ABH structures in air, resulting in a broadband reduction in structural vibration and sound radiation from the water-loaded ABH plate. © 2023 Acoustical Society of America. https://doi.org/10.1121/10.0020067

I. INTRODUCTION

Mitigating structural vibration and sound radiation is of great significance for many applications. As a novel, lightweight and effective passive solution, advanced structural design based on acoustic black hole (ABH) principles have been a subject of intense research over the past decade, as reviewed in a recent paper (Pelat *et al.*, 2020).

The pioneering work of Mironov (1988) and the experimental confirmation by Krylov and Winward (2007) both demonstrated that, as flexural waves propagate towards a one-dimensional (1D) wedge whose thickness is tailored according to a power–law variation, i.e., $h(x) = \varepsilon x^{\gamma}$ (with $\gamma \geq 2$), their phase velocity gradually slows down and the time taken to reach the edge tip would become infinite. This process neutralizes wave reflection at the edge tip and results in wave compression and energy concentration, which can be effectively absorbed by a small amount of damping materials deployed around the tip region. Based on this principle, extensive research has been conducted to explore the ABH-enabled benefits in terms of vibration and sound radiation reduction. Up until now, the problem has been predominantly addressed for structures in light fluid, such as air (Pelat *et al.*, 2020). In particular, using finite element (FE) models that consider the full fluid loading effects from the surrounding air, Conlon *et al.* (2015) first demonstrated that periodically embedded ABH plates can drastically reduce the vibration velocity and sound power. Tang *et al.* (2016) experimentally verified that ABH beams coated

with a damping layer entail largely increased system loss factors. Typical phenomena were also experimentally verified (Bowyer and Krylov, 2015; Ma and Cheng, 2019). Meanwhile, potential applications of the ABH have also been attempted (Prill and Busch, 2016).

Most existing analyses on ABH have been performed for light fluid (e.g., air), a topic that has been well mastered. Comparatively, exploration of ABH phenomena in heavy fluid receives little, if not completely inexistent, attention in the open literature. The topic, however, is of paramount importance for many underwater applications in which fluid–structure coupling needs to be considered. Although the issue has been well studied in classical vibro-acoustics involving conventional structures, like plates (Berry, 1990; Nelisse *et al.*, 1998) and shells (Laulagnet and Guyader, 1989; Dana *et al.*, 2020), it receives little attention in the context of ABH, which raises a series of intriguing yet important questions. More specifically, the structural specificity of the ABH structures, in terms of spatial wavelength variation and wave velocity changes, might challenge the common understandings on conventional or ABH structures, either in vacuum or immersed in light fluid, such as air. Meanwhile, due to the strong fluid–structural interaction, how the mass loading and radiation damping in heavy fluid would affect the ABH phenomena, as well as the sound radiation, remains obscure. These issues call for the development of efficient simulation tools as well as the assertion of typical ABH phenomena and their implication on vibration and sound radiation control applications. This forms the major motivation of the present work.

a)Electronic mail: li.cheng@polyu.edu.hk

The objectives of this paper are therefore twofold which show its novelty: (1) to establish an efficient simulation model to describe the vibro-acoustic behaviors of ABH plates coated with viscoelastic materials and immersed in heavy fluid, which calls for the rigorous consideration of strong fluid–structure coupling, (2) to examine whether ABH effects can still be materialized in heavy fluid (e.g., water), and if so, how the phenomena differ from the light fluid case (e.g., air) and what are the dominant factors that would impact on vibration and sound radiation in heavy fluid.

The remainder of the paper is organized as follows: in Sec. II, a semi-analytical model that considers the strong coupling between a simply supported ABH plate and its surrounding heavy fluid is proposed. The coupled model is then validated through comparisons with FE results in Sec. III. In Sec. IV, ABH-specific phenomena in water-loaded plates are scrutinized through examining some key vibro-acoustic indicators, with results cross-checked against their counterparts in air. In particular, numerical results are presented to show the effect of the fluid loading and that of the radiation damping on the vibrational behavior of the strongly coupled ABH plates in different frequency ranges. Finally, a summary is given in Sec. V.

II. SEMI-ANALYTICAL MODEL

We first present a semi-analytical model for the vibration and sound radiation analyses of a fluid-loaded ABH plate excited by transverse point forces. Figure 1 shows a rectangular, baffled plate for which the $z < 0$ infinite half-space is filled with a fluid (characterized by density ρ_f and sound speed c_f), while the $z > 0$ infinite half-space is *in vacuum*. Fluid loading effect is accounted for in the equation of motion of the plate so that light and heavy fluids can be managed. The investigated rectangular plate (with length a and width b) contains a circular indentation of radius R_{ABH} centered at (x_c, y_c). Both sides of the indented area are symmetrically
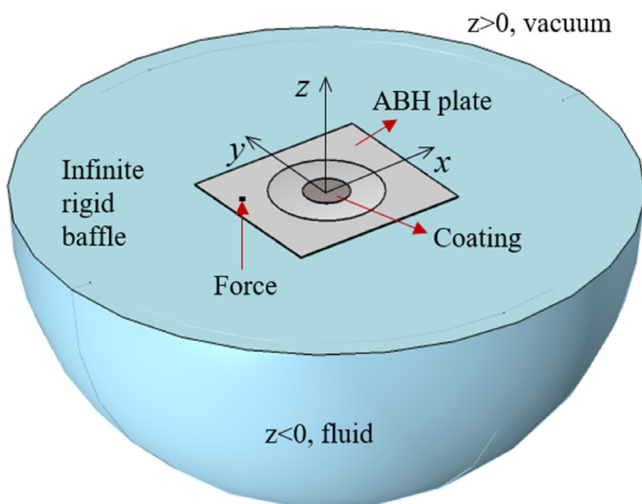

FIG. 1. (Color online) Coordinate system of an ABH plate inserted in an infinite rigid baffle.

coated with damping layers. The thickness of the uniform portion of the plate is h, while that of the ABH indentation follows $h(x,y) = \varepsilon\left(\sqrt{(x-x_c)^2 + (y-y_c)^2}\right)^{\gamma} + h_0$,   in which ε is a constant, γ is the power law index, and h_0 is the smallest residual thickness of the indentation at the center. Material damping is introduced through complex Young's modulus, i.e., $E_0^* = E_0(1 + i\eta_0)$ and $E_d^* = E_d(1 + i\eta_d)$, for the metal panel and the damping material, respectively, where η_0 and η_d represent their respective loss factors. Modal analyses on the plates with combined damping layers yield complex eigenvalues $\omega_d^2 = \omega_n^2(1 + i\eta_n)$, where η_n is the total loss factor of the entire structure. In principle, η_n includes the structural loss factor η_s and radiation loss factor η_r. While the latter might be negligible for light fluid, it might become important for heavy fluid. This will be dealt with in Sec. IV A.

The plate under investigation is assumed to be thin and symmetrical with respect to its mid-plane, for which case Kirchhoff's plate theory is valid. The displacement of the plate at a given point is written as

$$\{u, v, w\} = \left\{-z\frac{\partial w}{\partial x}, -z\frac{\partial w}{\partial y}, w\right\}, \tag{1}$$

where w is the transverse displacement, and u and v are the in-plane displacements in the x and y directions, respectively. Employing dimensionless coordinates $\bar{x} = x/a$ and $\bar{y} = y/b$, w can be expressed as

$$w = \sum_{m=1}^{N}\sum_{n=1}^{N} a_{mn}\varphi_m(\bar{x})\varphi_n(\bar{y}), \tag{2}$$

where $\varphi_m(\bar{x})$ and $\varphi_n(\bar{y})$ are the admissible functions in x and y directions, respectively, truncated to the order N. a_{mn} are the unknown complex coefficients and the generalized coordinates in the Euler–Lagrange equations resulting from the stationary state of the system:

$$Q_{mn} - \frac{d}{dt}\left(\frac{\partial T}{\partial \dot{a}_{mn}}\right) - \frac{\partial V}{\partial a_{mn}} + \frac{\partial W_{fluid}}{\partial a_{mn}} = 0, \tag{3}$$

where T and V are, respectively, the kinetic energy and potential energy of the plate, Q_{mn} is the generalized mechanical force, $\dot{a}_{mn}$ is the first order time derivative of the generalized coordinate a_{mn}, and W_{fluid} is the work done by fluid loading, which yields the generalized force from the surrounding fluid $f_{mn}^p = \partial W_{fluid}/\partial a_{mn} = i\omega\sum_p\sum_q Z_{mnpq}a_{mn}$. The determination of T and V can be found in the literature (O'Boy and Krylov, 2016). The acoustic pressure field should satisfy the continuity between the plate and the acoustic velocities at the interface:

$$v_n(x,y) = -\frac{1}{i\omega\rho_f}\frac{\partial p}{\partial z}\bigg|_{z=0}, \tag{4}$$

where v_n and p are the velocity and the acoustic pressure and ω is the circular frequency. Substituting the expressions

of the kinetic energy T, potential energy V, the work from the fluid loading W_{fluid}, and the generalized mechanical force Q_{mn} into Eq. (3) and assuming a harmonic state for the time dependence, $a = \mathbf{A}e^{i\omega t}$ yields a series of linear equations which can be cast into a matrix form as

$$(\mathbf{K} - \omega^2 \mathbf{M} + i\omega \mathbf{Z})\mathbf{A} = \mathbf{Q}, \tag{5}$$

where $\mathbf{K}$ and $\mathbf{M}$ are the stiffness and mass matrices, respectively, $\mathbf{Q}$ is the force vector of generalized mechanical force, and $\mathbf{A}$ is the amplitude of generalized coordinate. The derivations of $\mathbf{K}$, $\mathbf{M}$, and $\mathbf{Q}$ are detailed in Appendix A. $\mathbf{Z}$ is the sound radiation impedance matrix whose coefficients are

$$Z_{ijrs} = i\omega\rho_f \int\int_{S} \int_{S'} \varphi_{ij}(x',y')G(x',y',0;x,y,0)\varphi_{rs}(x,y)ds'ds, \tag{6}$$

where $G(x,y,0;x',y',0) = e^{-ikr}/2\pi r$ is the Green function for the semi-infinite free field with $r = \sqrt{(x-x')^2 + (y-y')^2}$.

The real part of $\mathbf{Z}$ is the radiation resistance which represents the radiation damping of the plate, while the imaginary part is the radiation reactance which represents the mass loading from the fluid on the plate. Equation (6) requires the evaluation of fourfold integrals. Employing an appropriate mapping of the coordinates, the fourfold integrals can be transformed into twofold integrals which can be evaluated using Gaussian quadrature scheme (see Appendix B). The topic was discussed in the literature (Sandman, 1975; Nelisse et al., 1998; Foin et al., 1999).

Dropping the mechanical excitation term in Eq. (5) yields a nonlinear eigenvalue problem. Employing the state-space coupling method, the implicit frequency of the radiation impedance $\mathbf{Z}$ is made explicit via a power series expansion over circular frequency (Giordano and Koopmann, 1995; Cunefare and De Rosa, 1999). In this case, the coupled system can be recast into a canonical state-space form as a standard eigenvalue problem. Solution to this problem produces complex eigenvalues and the corresponding system loss factors comprising structural loss factors and radiation loss factors. The solving procedure of this eigenvalue problem is detailed in Appendix C.

Upon obtaining the transverse vibration velocity of the fluid-loaded system under the excitation of mechanical forces, the sound pressure radiated into the fluid can be obtained (Fahy and Gardonio, 2007):

$$p(r) = \frac{i\omega\rho_f}{2\pi} \int\int_{S} v_n(r)\frac{e^{-ikr}}{r}dS, \tag{7}$$

where r is the position vector from a vibrating point to a receiver point in the far field and S is the surface of the vibrating plate. The sound power can then be computed:

$$W_{rad} = \int_0^{2\pi}\int_0^{\pi/2} \frac{|p(R_0,\theta,\phi)|^2}{2\rho_f c_f}r^2\sin\theta d\theta d\phi, \tag{8}$$

where R_0 is the radius of the integrating hemispherical surface, θ is the polar angle, and ϕ is the azimuth angle. For analysis, the radiation efficiency of the plate-fluid system is used, defined as

$$\sigma = \frac{W_{rad}}{\rho_f c_f S_v \langle|v_n|^2\rangle}, \tag{9}$$

where S_v is the surface area of the vibrating plate and $\langle|v_n|^2\rangle$ is the surface mean square velocity.

III. FEM VALIDATIONS

The accuracy of the proposed semi-analytical model is validated through comparisons with finite element method (FEM) simulations using COMSOL (Tabatabaian, 2014). Table I shows the geometric parameters of a simply supported steel ABH plate (density $\rho_0 = 7800$ kg/m³, Young's modulus $E_0 = 200$ GPa, material loss factor $\eta_0 = 0.01$, and Poisson's ratio $\mu_d = 0.33$). Herein, for the coating damping layer on each side of the plate, the thickness and radius are $3h_0$ and $0.408R_{ABH}$, respectively. Corresponding properties of the damping layers are $\rho_d = 950$ kg/m³, $E_d = 5$ GPa, $\eta_d = 0.3$, and $\mu_d = 0.33$.

Two admissible functions are implemented that satisfy the simply supported boundary conditions of the plate: $\varphi_m(\bar{x}) = \sin(m\pi\bar{x})$ and $\varphi_n(\bar{y}) = \sin(n\pi\bar{y})$. After a meticulous convergence study, $N = 40$ terms are used in each direction (x and y) to expand the plate displacement in Eq. (2). Corresponding FEM model is constructed using solid elements. The radius of the fluid domain is 810 mm with the outer layer (thickness 60 mm) tuned to be a perfectly matched layer (PML) that absorbs all outgoing waves without any impedance mismatch causing reflections at the boundary. The fluid is water with a density $\rho_f = 1000$ kg/m³ and sound speed $c_f = 1640$ m/s. The maximum element sizes of the uniform portion of the plate, ABH portion, and the fluid domain are 11.43, 2.85, and 37.5 mm, respectively, resulting in 6 47 565 domain elements in the FEM model. Applying a unit point force at $(x,y,z) = (-200, 90, 2.35)$ mm, the surface mean square velocity and radiated sound power of the fluid-loaded ABH plate are calculated and compared using the semi-analytical model and the FE model, as shown in Figs. 2(a) and 2(b), respectively. It can be seen that, despite the slight discrepancy at the first resonant peak, the agreement between the two models is good up to 3000 Hz. This indicates that the coupled matrix containing the radiation impedance coefficients is accurately computed in the current heavy fluid scenario, such as validating the semi-analytical model.

IV. NUMERICAL ANALYSES AND DISCUSSIONS

In this section, we elucidate the vibration and sound radiation behaviors of an ABH plate immersed in heavy fluid

TABLE I. Geometrical parameters of the ABH plate.

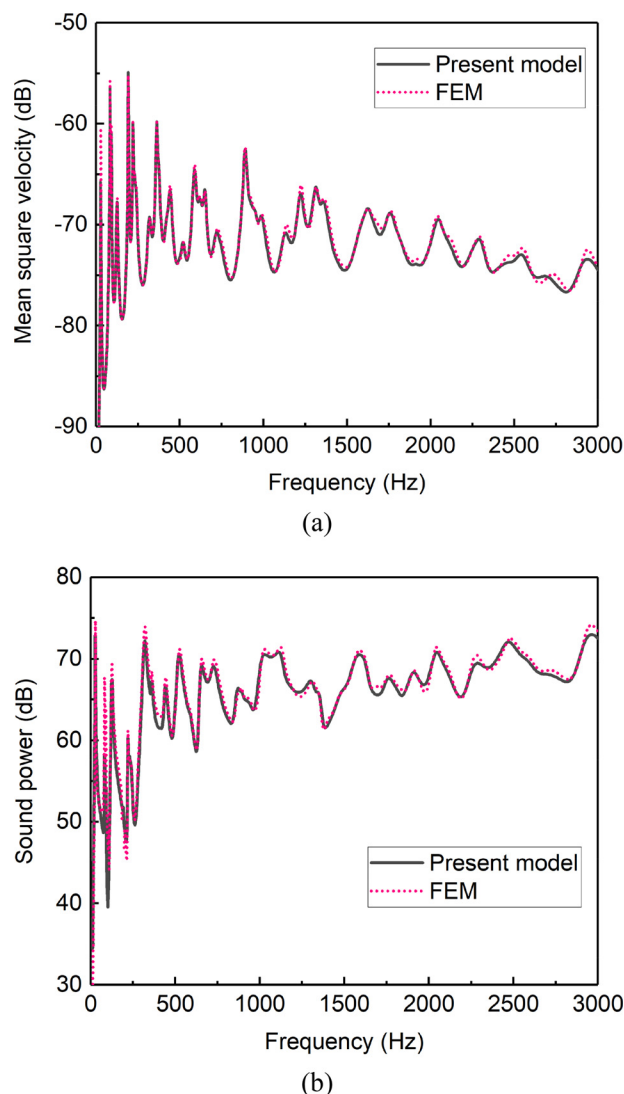| $a = 0.5$ m	$x_c = 0.25$ m	$\varepsilon = 0.2$/m
$b = 0.45$ m	$y_c = 0.2$ m	$\gamma = 2$
$h = 4.7$ mm	$h_0 = 0.2$ mm	$R_{ABH} = 0.15$ m

FIG. 2. (Color online) Comparisons of the mean square velocity and sound power for an ABH plate coated with damping layer in water between the present model (solid line) and FEM (dotted line). (a) Mean square velocity, (b) sound power.

(e.g., water) versus in light fluid (e.g., air). Vibro-acoustic metrics used for analyses include structural loss factors, surface mean square velocity, radiated sound power, and radiation efficiency. All geometrical and material parameters of the ABH plate are identical to those used in the previous case in Sec. III. A uniform plate coated with damping layers of the same configuration is also used as a reference.

A. ABH effect in heavy fluid

Largely enhanced structural loss factor is an important indicator of ABH effects as a result of energy focalization and dissipation. In a light fluid, structural loss factors can be computed directly from the standard complex eigenvalue problem (Ma *et al.*, 2018), while in heavy fluid, the solution to the eigenvalue problem leads to the total loss factors of the coupled system (see Appendix C). Therefore, in the latter case, the structural loss factors need to be extracted by

subtracting the radiation loss factors from the total damping factors as $\eta_s = \eta_t - \eta_r$, with η_s, η_t, and η_r being the structural loss factors, total loss factors, and radiation loss factors, respectively. The radiation loss factor quantifies the power lost to radiation, which is defined as (Hambric and Fahnline, 2007)

$$\eta_r = \frac{W_{rad}}{\omega W_{sys}}, \tag{10}$$

where W_{sys} is the system power which is twice of the kinetic energy.

Using a three-order interpolation (see Appendix C) of the radiation impedance, the state-space method employed to the eigenvalue problem of the coupled system would yield $7N^2$ eigenvalues and eigenvectors and only N^2 are physical (Cunefare and De Rosa, 1999; Li, 2005). There seems to be no eigenvalue theory that would allow one to analytically pick out the physical eigenvalues from the computed eigenvalues. In the present case, we use refined sweeping frequency (1 Hz resolution) to calculate the forced vibration responses and extract the resonant frequencies and the overall damping factors. Identified resonant frequencies from the forced vibration peaks are found to be a sub-set of the computed complex eigen-frequencies using the state-space method. As is known, with the same amount of damping material coated over the surface of an ABH indentation, the ABH plate is heavily damped, much more significantly than a uniform plate. Therefore, the method of selecting complex eigenvalues from the resonant peaks only allows the identification of the dominant modes (a sub-set of the entire structural modes) that contribute the most to the vibration response, which is sufficient to elucidate the dynamic features of the water-loaded plate. Solutions to the eigen-frequencies and the corresponding total loss factors can be found in Appendix C. Figure 3 compares the structural loss factors of dominant modes of the ABH plate in water, in comparison with those of its uniform counterpart below 3000 Hz. It shows that with the use of damping layers and the results compared with the intrinsic materialistic factors, structural loss factors of the uniform plate are only slightly increased, while those of the ABH plate are significantly increased to nearly four times. Additionally, the front view of the water-loaded vibration displacement maps at three typical resonant frequencies (318, 1222.2, and 2926 Hz) are also presented in Fig. 3. It can be seen that the vibration displacements inside the ABH indentation are drastically amplified, alongside a significant wavelength compression towards the ABH center, as exemplified by the front view of the vibration displacement at 1222.2 Hz. Meanwhile, distributions of the total system loss factors, structural loss factors, and radiation loss factors of the ABH plate are compared in Fig. 4. It shows that for the ABH plate in water, structural loss factors contribute the most to the total system loss factors. These results are the salient features that testify to the occurrence of ABH effects in heavy fluid.
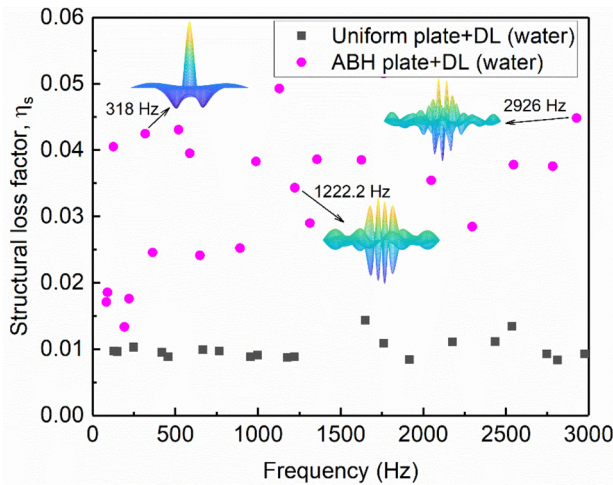
FIG. 3. (Color online) Structural loss factors of the dominant modes of structures in water. (a) Uniform plate (squares), (b) ABH plate (circles). DL denotes the coated damping layer.

B. Vibration and sound radiation characteristics

Vibration and sound radiation characteristics of air- and water-loaded ABH plates are then, respectively, investigated using the proposed semi-analytical model, with results compared with their uniorm counterparts. Figure 5(a) shows the mean square velocities of the ABH plate and its uniform counterpart, both in air. It follows that, compared with the uniform plate, the vibration of the ABH plate is largely reduced above the so called cut-on frequency (Conlon *et al.*, 2015), 504 Hz in the present case, at which the ABH effect begins to show systematically. However, an increase is also obvious below the cut-on frequency, all consistent with the common understanding reported in the literature for ABH structures without surrounding fluid (Conlon *et al.*, 2015; Ma *et al.*, 2018).

The phenomenon is then examined for the water-loaded plate in Fig. 5(b). It shows that above the cut-on frequency, the vibration of the ABH plate in water is heavily damped

(a)

(b)

FIG. 5. (Color online) Comparison of mean square velocity between uniform plate (dotted line) and ABH plate (solid line). (a) In air, (b) in water. DL denotes the coated damping layer. The green box highlights the resonant peaks at low frequencies for both plates.

compared with that of the uniform counterpart. The reduction in terms of the averaged mean square velocity is 1.7 dB larger than that in air [Fig. 5(a)]. Remarkably, below the cut-on frequency, the vibration of the water-loaded ABH plate is also reduced in most cases, which is different from what is observed for the plate in air. The reduction of the averaged mean square velocity amounts to roughly 2 dB larger than that in air. Similar phenomena (a reduction of 1.9 dB larger than in air) can be observed in terms of the radiated sound power (Fig. 6). The phenomena can be partly explained by the fact that the sound power of the ABH plate in water is significantly smaller than that of its uniform counterpart in the whole frequency range, which can be attributed to the reduced mean square velocity [Fig. 5(b)] and the reduced radiation efficiency [see Fig. 7(b)]. Also, as can be seen from Fig. 7(a), the radiation efficiencies of both plates in air steadily increase and remain high above the critical frequency (2554 Hz, estimated based on the thickness of the
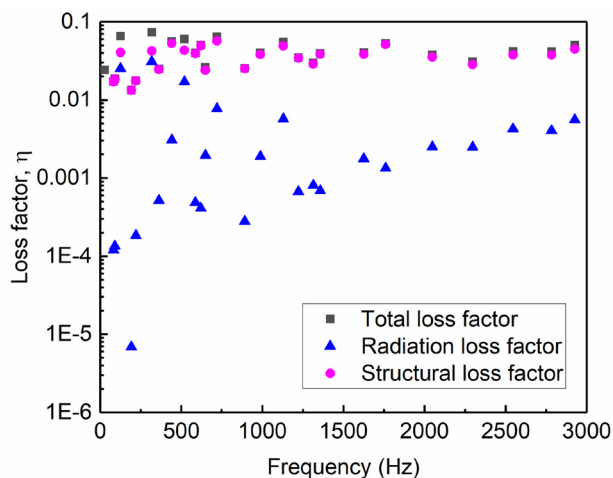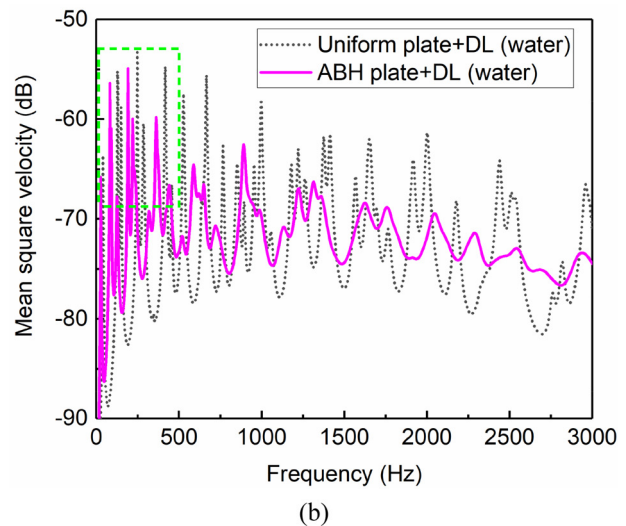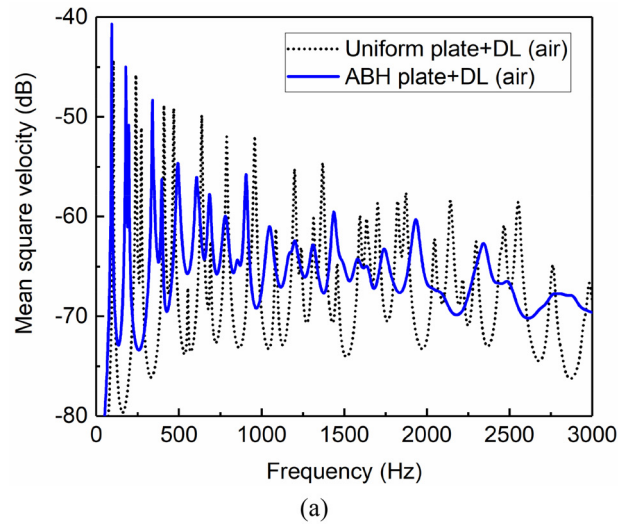

FIG. 4. (Color online) Loss factors of the dominant modes of an ABH plate coated with damping layer in water. (a) Total loss factor (squares), (b) radiation loss factor (triangles), (c) structural loss factor (circles).
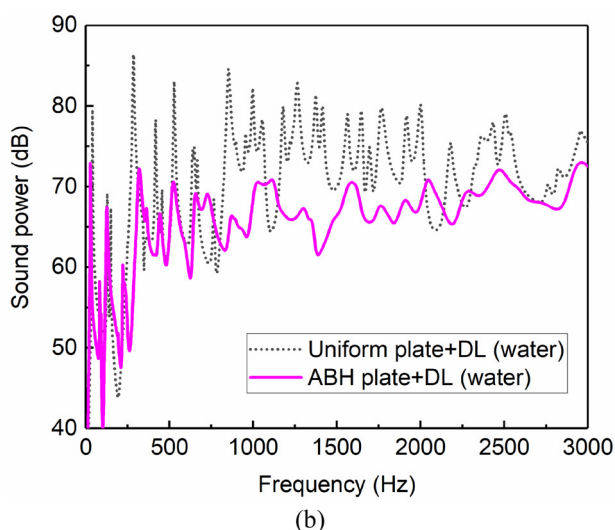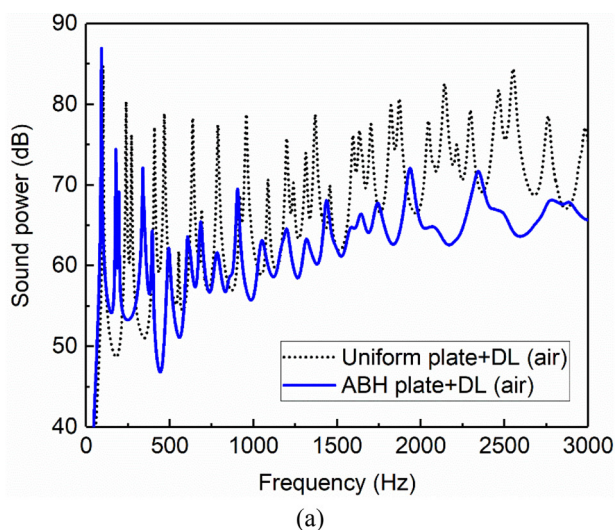
FIG. 6. (Color online) Comparison of radiated sound power between the uniform plate (dotted line) and the ABH plate (solid line). (a) In air, (b) in water. DL denotes the coated damping layer.
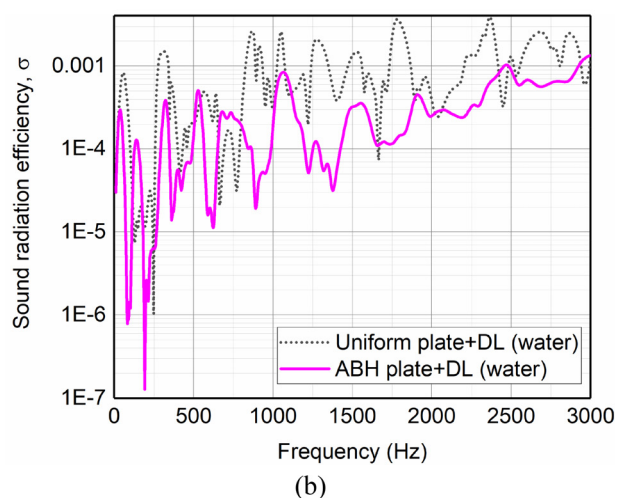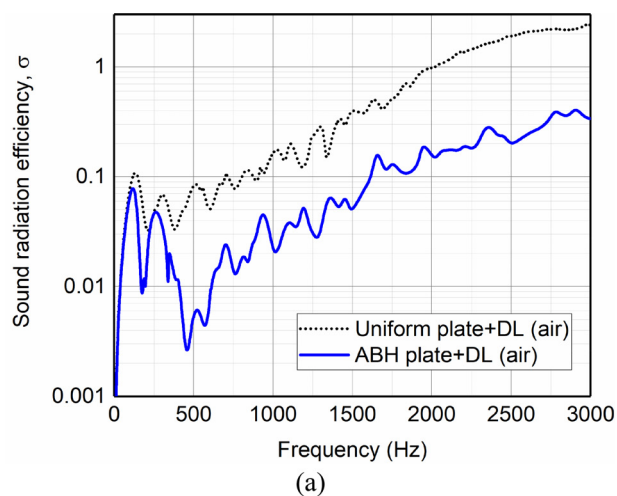

FIG. 7. (Color online) Comparison of radiation efficiency between the uniform plate (dotted line) and the ABH plate (solid line). (a) In air, (b) in water. DL denotes the coated damping layer.

uniform part of the plate), while in water, they fluctuate [see Fig. 7(b)] as the critical frequency in water far exceeds that in air. All of these factors echo the observation that there is a substantial reduction in vibration and sound radiation of the ABH plate in water, compared with its uniform counterpart, and the reduction is obvious compared with the case in air.

A closer examination is conducted to better understand the differences of the ABH effects on plates in water and in air. Figure 8 shows the mean square velocity for the uniform plate [see Fig. 8(a)] and that of the ABH plate [see Fig. 8(b)], immersed in air and water, respectively. For both plates, one can see a clear downshifting of the resonant frequencies due to the mass loading effect which is more significant from water. On the other hand, compared with the air case, the vibration of the ABH plate in water is heavily damped, yielding a reduction up to 10 dB in the mid-to-high frequency range, much more visible than that of the uniform plate. To explain these phenomena and understand the underlying mechanisms, the effect of the radiation damping

and that of the mass loading on vibration responses of the ABH plate and the uniform plate are scrutinized hereafter.

C. Effects of radiation damping and mass loading on vibration response

In contrast to the light fluid case, two dominant phenomena feature the heavy fluid effects on the plate: mass loading effect (mainly in low-frequency range) and radiation damping effect (mainly in high frequency range). To assess their respective importance in the context of ABH plates, the real and imaginary parts of the radiation impedance $\mathbf{Z}$ are separately considered in Eq. (5) to analyze the effects of radiation damping and mass loading on the mean square velocity of an ABH plate in water [Fig. 9(b)], in comparison with the uniform plate [Fig. 9(a)].

Figure 9(a) shows that with radiation damping, the vibration response of the uniform plate at resonant peaks is evidently reduced, in contrast to the case without radiation damping, especially in the mid-to-high frequency range. This observation agrees with the results obtained by Foin (1999). However, the radiation damping has little influence on the vibration response of the ABH plate, as shown in Fig. 9(b). This is because the
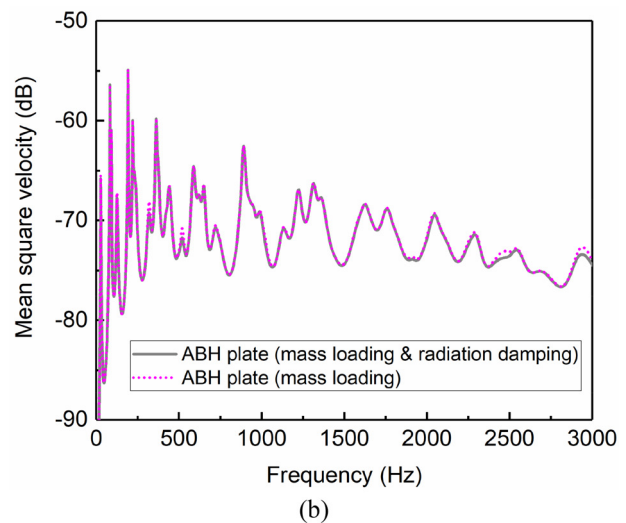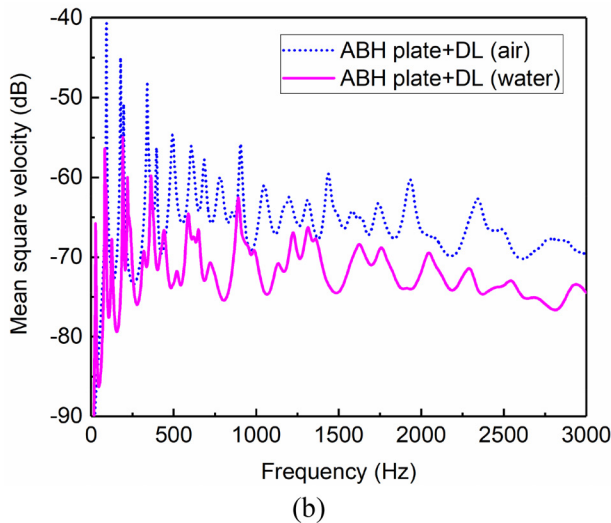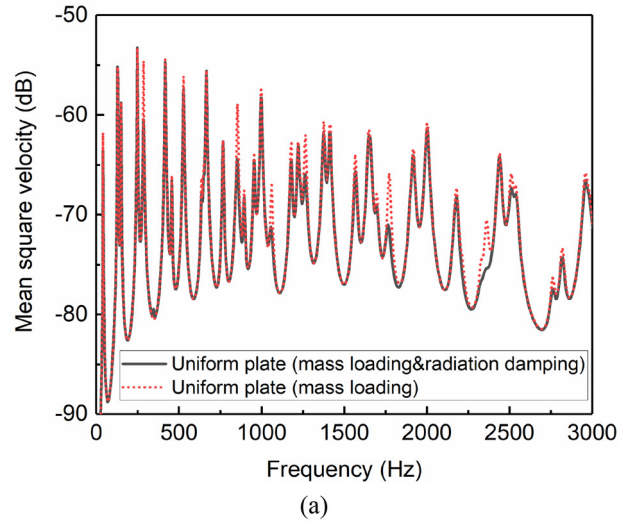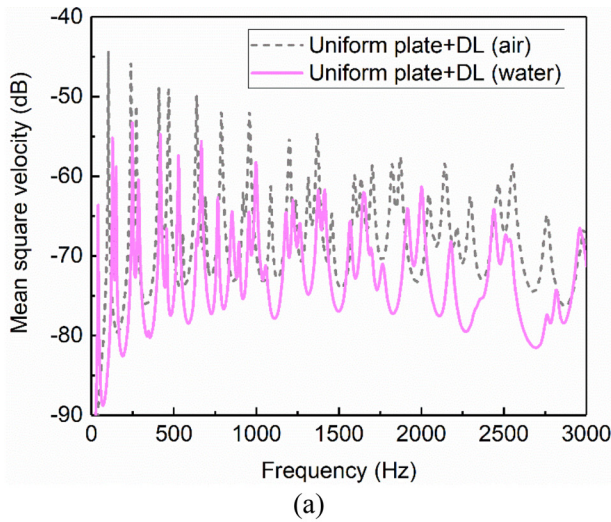
FIG. 8. (Color online) Comparison of mean square velocity in air and in water. (a) Uniform plate, (b) ABH plate. DL denotes the coated damping layer.

FIG. 9. (Color online) Effect of radiation damping on mean square velocity: (a) Uniform plate, (b) ABH plate.

structural damping, which is significantly enhanced by the ABH effects as a result of energy focalization and dissipation, overwhelms the radiation damping (see Fig. 4).

Furthermore, comparisons of radiation damping effect on vibration responses between the ABH plate and its uniform counterpart are presented in Fig. 10(a). It merely shows that with the radiation damping effect without the mass loading effect, the resonant peak levels of the ABH plate are larger than that of the uniform plate in the low-frequency range (typically below 500 Hz). This is because radiation damping is more significant for the vibration reduction of the uniform plate in the higher frequency range, while it is less predominant in the case of the ABH plate.

Additionally, comparisons of mass loading effect between the ABH plate and its uniform counterpart are presented in Fig. 10(b). It seems that, different from radiation damping effect in Fig. 10(a), the resonant peaks (of the mass loading effect) of the ABH plate are less energetic than those of the uniform plate almost in the whole frequency range. Focusing on the low-frequency range, the observed

reduction is attributed to the mass loading effects from the fluid, which is more significant on the ABH plate due to the reducing thickness of the ABH indentation. These results indicate that in heavy fluid, the mass loading effect can compensate for the low-frequency deficiency of the air-loaded ABH structures. In the mid-to-high frequency range, the considerable vibration reduction is attributed to the combined effects of mass loading and the ABH effects. These parametric analyses provide a physical insight into the vibration reduction behaviors of ABH plates in heavy fluid.

V. CONCLUSIONS

This paper is dedicated to the study of vibration and sound radiation characteristics of ABH plates in either light or heavy fluid. A general semi-analytical model is presented alongside a Rayleigh–Ritz procedure to simulate the dynamics of a simply supported plate radiating sound into an infinite surrounding medium. FEM results are presented to validate the accuracy of the model in a strongly coupled

J. Acoust. Soc. Am. **154** (1), July 2023
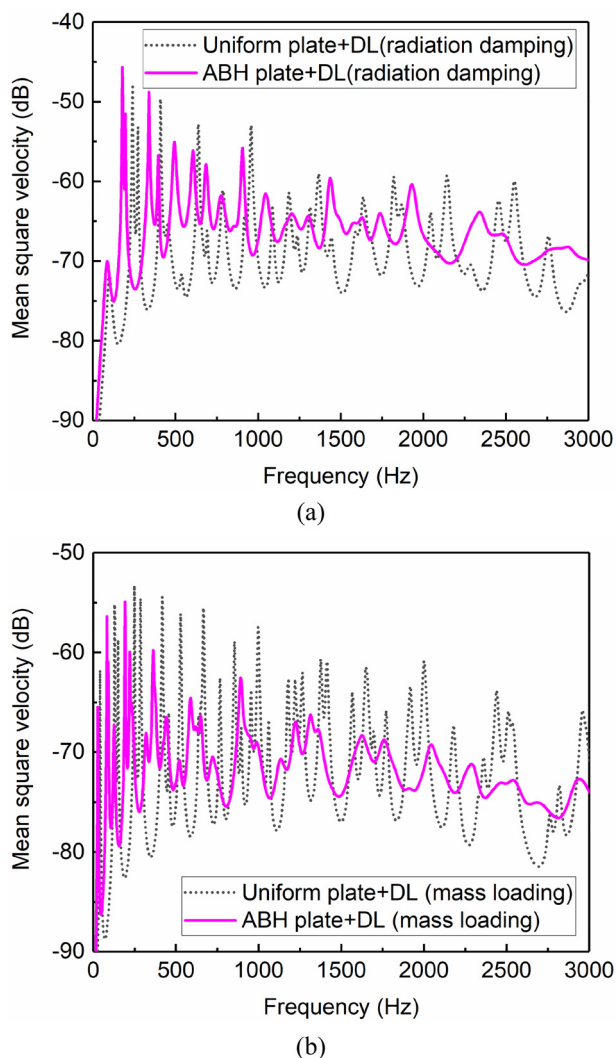
Li Ma and Li Cheng   185

FIG. 10. (Color online) Effect of mass loading on mean square velocity. (a) Uniform plate, (b) ABH plate. DL denotes the coated damping layer.

context. Meanwhile, vibration and sound radiation behaviors of the ABH plate in water versus in air are analyzed and discussed with significant differences highlighted and mechanisms elucidated. Drawn from the simulated cases and analyses, main conclusions are summarized as follows:

(1) The proposed semi-analytical model can handle the vibration and sound radiation of an ABH plate in heavy fluid, for which fluid–structure coupling needs to be rigorously considered. Good agreement is found between the proposed model and FEM simulations in the strong coupling context.

(2) ABH effects can be systematically materialized in heavy fluid, as evidenced by the increased structural loss factors and reduced mean square velocity of the ABH plates and its impaired sound radiation efficiency and sound power. In water, radiation damping, which plays an important role in the case of uniform plate, is only a minor part in the overall system damping in an ABH plate due to the overwhelming structural damping, which is significantly enhanced by ABH effects.

(3) With the same damping treatment, a water-loaded ABH plate entails a more significant and systematic vibration reduction than its counterpart in air. More remarkably, the well-acknowledged low-frequency deficiency of the air-loaded ABH structures (in terms of vibration increase) can be alleviated by the enhanced mass loading effects coming from the water, which is more significant than air. Note, however, that the fluid loading effect cannot directly overcome the low-frequency deficiency of the ABH effect. Instead, due to the reducing thickness in the ABH indentation, ABH plates are thinner than their uniform counterparts. As a result, the overall damping of the ABH plates is higher than that of the uniform plates in the low-frequency range, conducive to vibration reduction. Alongside the ABH-induced effects above the cut-on frequency, this results in a cross-frequency and wide-band vibration and sound radiation reduction of the water-loaded plate.

APPENDIX A: DETERMINATION OF M, K, AND Q MATRICES

The plate structure is divided into five parts: uniform parts from 1 to 4 and an ABH part 5. The part coated with damping layers is numbered 6 (Fig. 11):

$$\mathbf{M} = \mathbf{M}^{Uniform} + \mathbf{M}^{ABH} + \mathbf{M}^{Damping},$$

$$\mathbf{K} = \mathbf{K}^{Uniform} + \mathbf{K}^{ABH} + \mathbf{K}^{Damping},$$
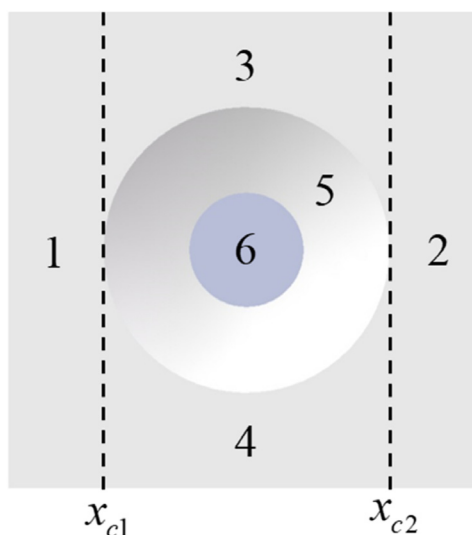

FIG. 11. (Color online) Division of a circular ABH plate.

$$\mathbf{M}^{Uniform} = \rho h a b \left(\begin{array}{c} \int_0^1 \int_0^{\bar{x}_{c1}} \varphi_m(\bar{x})\varphi_p(\bar{x})\varphi_n(\bar{y})\varphi_q(\bar{y})d\bar{x}d\bar{y} + \int_0^1 \int_{\bar{x}_{c2}}^1 \varphi_m(\bar{x})\varphi_p(\bar{x})\varphi_n(\bar{y})\varphi_q(\bar{y})d\bar{x}d\bar{y} \\ + \int_{\bar{y}_r - \frac{1}{b}\sqrt{(R_{ABH})^2 - a^2(\bar{x}-\bar{x}_r)^2}}^1 \int_{\bar{x}_{c1}}^{\bar{x}_{c2}} \varphi_m(\bar{x})\varphi_p(\bar{x})\varphi_n(\bar{y})\varphi_q(\bar{y})d\bar{x}d\bar{y} \\ + \int_0^{\bar{y}_r + \frac{1}{b}\sqrt{(R_{ABH})^2 - a^2(\bar{x}-\bar{x}_r)^2}} \int_{\bar{x}_{c1}}^{\bar{x}_{c2}} \varphi_m(\bar{x})\varphi_p(\bar{x})\varphi_n(\bar{y})\varphi_q(\bar{y})d\bar{x}d\bar{y} \end{array} \right) = \rho h a b \sum_{q=1}^4 \left(\mathbf{I}_{x_q}^{00} \otimes \mathbf{I}_{y_q}^{00} \right),$$

$$\mathbf{M}^{ABH} = \rho a b \left(\int_{\bar{y}_r - \frac{1}{b}\sqrt{(R_{ABH})^2 - a^2(\bar{x}-\bar{x}_r)^2}}^{\bar{y}_r + \frac{1}{b}\sqrt{(R_{ABH})^2 - a^2(\bar{x}-\bar{x}_r)^2}} \int_{\bar{x}_{c1}}^{\bar{x}_{c2}} h(\bar{x},\bar{y})\varphi_m(\bar{x})\varphi_p(\bar{x})\varphi_n(\bar{y})\varphi_q(\bar{y})d\bar{x}d\bar{y} \right) = \rho a b \left(\mathbf{I}_{5,mpnq}^{0000} \right),$$

$$\mathbf{M}^{Damping} = \rho a b \left(\int_{\bar{y}_r - \frac{1}{b}\sqrt{(R_d)^2 - a^2(\bar{x}-\bar{x}_r)^2}}^{\bar{y}_r + \frac{1}{b}\sqrt{(R_d)^2 - a^2(\bar{x}-\bar{x}_r)^2}} \int_{\bar{x}_{d1}}^{\bar{x}_{d2}} h_d \varphi_m(\bar{x})\varphi_p(\bar{x})\varphi_n(\bar{y})\varphi_q(\bar{y})d\bar{x}d\bar{y} \right) = \rho a b \mathbf{I}_{x_d}^{00} \otimes \mathbf{I}_{y_d}^{00},$$

$$\mathbf{K}^{Uniform} = D \cdot \frac{b}{a^3} \left(\begin{array}{c} \int_0^1 \int_0^{\bar{x}_{c1}} \varphi_m''(\bar{x})\varphi_p''(\bar{x})\varphi_n(\bar{y})\varphi_q(\bar{y})d\bar{x}d\bar{y} + \int_0^1 \int_{\bar{x}_{c2}}^1 \varphi_m''(\bar{x})\varphi_p''(\bar{x})\varphi_n(\bar{y})\varphi_q(\bar{y})d\bar{x}d\bar{y} \\ + \int_{\bar{y}_r - \frac{1}{b}\sqrt{(R_{ABH})^2 - a^2(\bar{x}-\bar{x}_r)^2}}^1 \int_{\bar{x}_{c1}}^{\bar{x}_{c1}} \varphi_m''(\bar{x})\varphi_p''(\bar{x})\varphi_n(\bar{y})\varphi_q(\bar{y})d\bar{x}d\bar{y} \\ + \int_0^{\bar{y}_r + \frac{1}{b}\sqrt{(R_{ABH})^2 - a^2(\bar{x}-\bar{x}_r)^2}} \int_{\bar{x}_{c1}}^{\bar{x}_{c1}} \varphi_m''(\bar{x})\varphi_p''(\bar{x})\varphi_n(\bar{y})\varphi_q(\bar{y})d\bar{x}d\bar{y} \end{array} \right)$$

$$+ D \cdot \frac{a}{b^3} \left(\begin{array}{c} \int_0^1 \int_0^{\bar{x}_{c1}} \varphi_m(\bar{x})\varphi_p(\bar{x})\varphi_n''(\bar{y})\varphi_q''(\bar{y})d\bar{x}d\bar{y} + \int_0^1 \int_{\bar{x}_{c2}}^1 \varphi_m(\bar{x})\varphi_p(\bar{x})\varphi_n''(\bar{y})\varphi_q''(\bar{y})d\bar{x}d\bar{y} \\ + \int_{\bar{y}_r - \frac{1}{b}\sqrt{(R_{ABH})^2 - a^2(\bar{x}-\bar{x}_r)^2}}^1 \int_{\bar{x}_{c1}}^{\bar{x}_{c1}} \varphi_m(\bar{x})\varphi_p(\bar{x})\varphi_n''(\bar{y})\varphi_q''(\bar{y})d\bar{x}d\bar{y} \\ + \int_0^{\bar{y}_r + \frac{1}{b}\sqrt{(R_{ABH})^2 - a^2(\bar{x}-\bar{x}_r)^2}} \int_{\bar{x}_{c1}}^{\bar{x}_{c1}} \varphi_m(\bar{x})\varphi_p(\bar{x})\varphi_n''(\bar{y})\varphi_q''(\bar{y})d\bar{x}d\bar{y} \end{array} \right)$$

$$+ \frac{\mu_0 D}{ab} \left(\begin{array}{c} \int_0^1 \int_0^{\bar{x}_{c1}} \varphi_m''(\bar{x})\varphi_p(\bar{x})\varphi_n(\bar{y})\varphi_q''(\bar{y})d\bar{x}d\bar{y} + \int_0^1 \int_{\bar{x}_{c2}}^1 \varphi_m''(\bar{x})\varphi_p(\bar{x})\varphi_n(\bar{y})\varphi_q''(\bar{y})d\bar{x}d\bar{y} \\ + \int_{\bar{y}_r - \frac{1}{b}\sqrt{(R_{ABH})^2 - a^2(\bar{x}-\bar{x}_r)^2}}^1 \int_{\bar{x}_{c1}}^{\bar{x}_{c1}} \varphi_m''(\bar{x})\varphi_p(\bar{x})\varphi_n(\bar{y})\varphi_q''(\bar{y})d\bar{x}d\bar{y} \\ + \int_0^{\bar{y}_r + \frac{1}{b}\sqrt{(R_{ABH})^2 - a^2(\bar{x}-\bar{x}_r)^2}} \int_{\bar{x}_{c1}}^{\bar{x}_{c1}} \varphi_m''(\bar{x})\varphi_p(\bar{x})\varphi_n(\bar{y})\varphi_q''(\bar{y})d\bar{x}d\bar{y} \end{array} \right)$$

$$+ \frac{2(1-\mu_0)D}{ab} \left(\begin{array}{c} \int_0^1 \int_0^{\bar{x}_{c1}} \varphi_m'(\bar{x})\varphi_p'(\bar{x})\varphi_n'(\bar{y})\varphi_q'(\bar{y})d\bar{x}d\bar{y} + \int_0^1 \int_{\bar{x}_{c2}}^1 \varphi_m'(\bar{x})\varphi_p'(\bar{x})\varphi_n'(\bar{y})\varphi_q'(\bar{y})d\bar{x}d\bar{y} \\ + \int_{\bar{y}_r - \frac{1}{b}\sqrt{(R_{ABH})^2 - a^2(\bar{x}-\bar{x}_r)^2}}^1 \int_{\bar{x}_{c1}}^{\bar{x}_{c1}} \varphi_m'(\bar{x})\varphi_p'(\bar{x})\varphi_n'(\bar{y})\varphi_q'(\bar{y})d\bar{x}d\bar{y} \\ + \int_0^{\bar{y}_r + \frac{1}{b}\sqrt{(R_{ABH})^2 - a^2(\bar{x}-\bar{x}_r)^2}} \int_{\bar{x}_{c1}}^{\bar{x}_{c1}} \varphi_m'(\bar{x})\varphi_p'(\bar{x})\varphi_n'(\bar{y})\varphi_q'(\bar{y})d\bar{x}d\bar{y} \end{array} \right)$$

$$= D \cdot \frac{b}{a^3} \left(\sum_{q=1}^4 \mathbf{I}_{x_q}^{22} \otimes \mathbf{I}_{y_q}^{00} \right) + D \cdot \frac{a}{b^3} \left(\sum_{q=1}^4 \mathbf{I}_{x_q}^{00} \otimes \mathbf{I}_{y_q}^{22} \right) + \mu_0 D \cdot \frac{1}{ab} \left(\sum_{q=1}^4 \mathbf{I}_{x_q}^{20} \otimes \mathbf{I}_{y_q}^{02} \right) + 2(1-\mu_0)D \cdot \frac{1}{ab} \left(\sum_{q=1}^4 \mathbf{I}_{x_q}^{11} \otimes \mathbf{I}_{y_q}^{11} \right),$$

$$\mathbf{K}^{ABH} = \frac{E_0}{12(1-\mu_0^2)} \left\{ \int_{\bar{y}_r - \frac{1}{b}\sqrt{(R_{ABH})^2 - a^2(\bar{x}-\bar{x}_r)^2}}^{\bar{y}_r + \frac{1}{b}\sqrt{(R_{ABH})^2 - a^2(\bar{x}-\bar{x}_r)^2}} \int_{\bar{x}_{c1}}^{\bar{x}_{c1}} [h(\bar{x},\bar{y})]^3 \begin{pmatrix} \frac{b}{a^3}\varphi_m''(\bar{x})\varphi_p''(\bar{x})\varphi_n(\bar{y})\varphi_q(\bar{y}) \\ + \frac{a}{b^3}\varphi_m(\bar{x})\varphi_p(\bar{x})\varphi_n''(\bar{y})\varphi_q''(\bar{y}) \\ + \frac{\mu_0}{ab}\varphi_m''(\bar{x})\varphi_p(\bar{x})\varphi_n(\bar{y})\varphi_q''(\bar{y}) \\ + \frac{2(1-\mu_0)}{ab}\varphi_m'(\bar{x})\varphi_p'(\bar{x})\varphi_n'(\bar{y})\varphi_q'(\bar{y}) \end{pmatrix} d\bar{x}d\bar{y} \right\}$$

$$= \frac{E_0}{12(1-\mu_0^2)} \left\{ \frac{b}{a^3}\left(\mathbf{I}_{5,mpnq}^{2200}\right) + \frac{a}{b^3}\left(\mathbf{I}_{5,mpnq}^{0022}\right) + \frac{\mu_0}{ab}\left(\mathbf{I}_{5,mpnq}^{2002}\right) + \frac{2(1-\mu_0)}{ab}\left(\mathbf{I}_{5,mpnq}^{1111}\right) \right\},$$

$$\mathbf{K}^{Damping} = \frac{E_d}{12(1-\mu_d^2)} \left\{ \int_{\bar{y}_r - \frac{1}{b}\sqrt{(R_d)^2 - a^2(\bar{x}-\bar{x}_r)^2}}^{\bar{y}_r + \frac{1}{b}\sqrt{(R_d)^2 - a^2(\bar{x}-\bar{x}_r)^2}} \int_{\bar{x}_{d1}}^{\bar{x}_{d2}} \left\{ [2h_d + h(\bar{x})]^3 - [h(\bar{x})]^3 \right\} \begin{pmatrix} \frac{b}{a^3}\varphi_m''(\bar{x})\varphi_p''(\bar{x})\varphi_n(\bar{y})\varphi_q(\bar{y}) \\ + \frac{a}{b^3}\varphi_m(\bar{x})\varphi_p(\bar{x})\varphi_n''(\bar{y})\varphi_q''(\bar{y}) \\ + \frac{\mu_d}{ab}\varphi_m''(\bar{x})\varphi_p(\bar{x})\varphi_n(\bar{y})\varphi_q''(\bar{y}) \\ + \frac{2(1-\mu_d)}{ab}\varphi_m'(\bar{x})\varphi_p'(\bar{x}) \\ \times \varphi_n'(\bar{y})\varphi_q'(\bar{y}) \end{pmatrix} d\bar{x}d\bar{y} \right\}$$

$$= \frac{E_d}{6(1-\mu_d^2)} \left\{ \frac{b}{a^3}\left(\mathbf{I}_{6,mpnq}^{2200}\right) + \frac{a}{b^3}\left(\mathbf{I}_{6,mpnq}^{0022}\right) + \frac{\mu_d}{ab}\left(\mathbf{I}_{6,mpnq}^{2002}\right) + \frac{2(1-\mu_d)}{ab}\left(\mathbf{I}_{6,mpnq}^{1111}\right) \right\}.$$

The quadrature integrals in $\mathbf{K}$ and $\mathbf{M}$ can be calculated using 2D Gaussian integral scheme.

The generalized mechanical force is written as

$$\mathbf{Q}_{mn} = \mathbf{Q}_A \varphi_m(\bar{x})\varphi_n(\bar{y}),$$

where $\mathbf{Q}_A$ is the amplitude of the mechanical force.

APPENDIX B: CALCULATION OF THE RADIATION IMPEDANCE

The components of the radiation impedance matrix are

$$Z_{mnpq} = i\omega\rho_f \int_s \int_{s'} \varphi_{mn}(x',y') G(x',y',0;x,y,0)\varphi_{pq}(x,y)ds'ds, \tag{B1}$$

where the Green function is $G = e^{-ikr}/2\pi r$ and $r = \sqrt{(x-x')^2 + (y-y')^2}$.

Assuming $\alpha = 2x/a, \beta = 2y/b$, and $\alpha' = 2x'/a, \beta' = 2y'/b$, the impedance terms can be transformed in the form

$$Z_{mnpq} = i\omega\rho_f \frac{ab^2}{4\pi} \int_{-1}^{1} \int_{-1}^{1} F_{mp}(u)K(u,u')F_{nq}(u')dudu' \tag{B2}$$

in which $F_{mp}(u)$ and $K(u,u')$ are

$$F_{mp}(u) = \frac{2}{\pi} \left[\frac{\cos\left(\frac{m-p}{2}\pi + \frac{m+p}{4}\pi(u+1)\right)\sin\left(\frac{m-p}{2}\pi - \frac{m-p}{4}\pi(u+1)\right)}{m-p} - \frac{\cos\left(\frac{m+p}{2}\pi + \frac{m-p}{4}\pi(u+1)\right)\sin\left(\frac{m+p}{2}\pi - \frac{m+p}{4}\pi(u+1)\right)}{m+p} \right]$$

and $K(u,u') = e^{-i(k_0 a/2)r}/r$, respectively, where $r = [(u+1)^2 + (u'+1)^2/r_0^2]^{1/2}$ with $r_0 = a/b$.

When $m = p$, $F_{mp}(u)$ becomes

$$F_{mp}(u) = \left(1 - \frac{u+1}{2}\right)\cos\left(\frac{m+p}{4}\pi(u+1)\right) - \frac{2}{\pi}\frac{\cos\left(\frac{m+p}{2}\pi\right)\sin\left(\frac{m+p}{2}\pi - \frac{m+p}{4}\pi(u+1)\right)}{m+p}. \tag{B3}$$

When $m + p$ or $n + q$ is odd, $F_{mp}(u) = F_{pm}(u) = F_{nq}(u') = F_{qn}(u') = 0$.

Li Ma and Li Cheng

APPENDIX C: SOLUTION TO THE EIGENVALUE PROBLEM OF THE COUPLED SYSTEM

$K(u, u')$ in Eq. (B2) can be expressed as

$$K(u, u') = \frac{1}{r}\left(\cos\left(\frac{k_0 a}{2}r\right) - i\sin\left(\frac{k_0 a}{2}r\right)\right), \quad \text{(C1)}$$

where $k_0 = \omega/c_0$. Expanding the real part of Z_{mnpq} into a power series, truncated up to three terms:

$$
\begin{aligned}
Z_{mnpq}(R) &= \omega\rho_f \frac{ab^2}{4\pi}\int_{-1}^{1}\int_{-1}^{1} F_{mp}(u)F_{nq}(u') \\
&\quad \times \frac{1}{r}\sin\left(\omega\cdot\frac{ar}{2c_0}\right)dudu' \\
&= \omega\rho_f \frac{ab^2}{4\pi}\int_{-1}^{1}\int_{-1}^{1} F_{mp}(u)F_{nq}(u')\frac{1}{r}\left(\left(\omega\cdot\frac{ar}{2c_0}\right)\right. \\
&\quad \left. -\frac{1}{3!}\left(\omega\cdot\frac{ar}{2c_0}\right)^3 + \frac{1}{5!}\left(\omega\cdot\frac{ar}{2c_0}\right)^5\right)dudu' \\
&= \omega^2 Z_{R2,mnpq} + \omega^4 Z_{R4,mnpq} + \omega^6 Z_{R6,mnpq}, \quad \text{(C2)}
\end{aligned}
$$

where

$$
\begin{aligned}
Z_{R(2k),mnpq} &= \rho_f \frac{ab^2}{4\pi}\int_{-1}^{1}\int_{-1}^{1} F_{mp}(u)F_{nq}(u')\frac{1}{r} \\
&\quad \times \left(\frac{(-1)^{k-1}}{2k-1}\left(\frac{ar}{2c_0}\right)^{2k-1}\right)dudu', \quad k=1,2,3.
\end{aligned}
$$
$$\text{(C3)}$$

Similarly, the imaginary part of Z_{mnpq} can be expressed as

$$Z_{mnpq}(I) = \omega Z_{I1,mnpq} + \omega^3 Z_{I3,mnpq} + \omega^5 Z_{I5,mnpq}, \quad \text{(C4)}$$

where

$$
\begin{aligned}
Z_{I(2k+1),mnpq} &= \rho_f(ab^2/4\pi)\int_{-1}^{1}\int_{-1}^{1} F_{mp}(u)F_{nq}(u')1/r \\
&\quad \times ((-1)^k/(2k)!(ar/2c_0)^{2k})dudu' \quad k=0,1,2.
\end{aligned}
$$

Z_{mnpq} can then be written as

$$
\begin{aligned}
Z_{mnpq} &= \left(\omega^2 Z_{R2,mnpq} + \omega^4 Z_{R4,mnpq} + \omega^6 Z_{R6,mnpq}\right) \\
&\quad + i\left(\omega Z_{I1,mnpq} + \omega^3 Z_{I3,mnpq} + \omega^5 Z_{I5,mnpq}\right). \quad \text{(C5)}
\end{aligned}
$$

Assuming the generalized displacement $\mathbf{a} = \mathbf{A}e^{i\omega t}$ leads to $\omega^n = 1/\mathbf{a}\left(\mathbf{a}^{(n)}/i^n\right)$ and yields:

$$
\begin{aligned}
i\omega Z_{mnpq}\mathbf{a} &= (-Z_{R6,mnpq})\mathbf{a}^{(7)} + (Z_{I5,mnpq})\mathbf{a}^{(6)} \\
&\quad + (Z_{R4,mnpq})\mathbf{a}^{(5)} + (-Z_{I3,mnpq})\mathbf{a}^{(4)} \\
&\quad + (-Z_{R2,mnpq})\mathbf{a}^{(3)} + (Z_{I1,mnpq})\mathbf{a}^{(2)}. \quad \text{(C6)}
\end{aligned}
$$

The eigenvalue equation $\mathbf{M\ddot{a}} + \mathbf{Ka} + i\omega\mathbf{Za} = 0$ can be transformed into the form $\mathbf{B\dot{y}} + \mathbf{Cy} = 0$. Assuming $\mathbf{y} = \mathbf{Y}e^{i\omega t}$ yields

$$-\mathbf{Cy} = (i\omega)\mathbf{By}, \quad \text{(C7)}$$

where $\mathbf{y} = \left\{\mathbf{a}^{(6)T}\ \mathbf{a}^{(5)T}\ \mathbf{a}^{(4)T}\ \mathbf{a}^{(3)T}\ \mathbf{a}^{(2)T}\ \mathbf{a}^{(1)T}\right\}^{T}$ and the super-script T represents the transpose. The solution to Eq. (C7) yields the complex eigen-frequencies and the corresponding system loss factors. Matrices $\mathbf{B}$ and $\mathbf{C}$ are

$$
\mathbf{B} = \begin{bmatrix}
-\mathbf{Z_{R6}} & 0 & 0 & 0 & 0 & 0 & 0 \\
0 & \mathbf{I} & 0 & 0 & 0 & 0 & 0 \\
0 & 0 & \mathbf{I} & 0 & 0 & 0 & 0 \\
0 & 0 & 0 & \mathbf{I} & 0 & 0 & 0 \\
0 & 0 & 0 & 0 & \mathbf{I} & 0 & 0 \\
0 & 0 & 0 & 0 & 0 & \mathbf{I} & 0 \\
0 & 0 & 0 & 0 & 0 & 0 & \mathbf{I}
\end{bmatrix} \quad \text{(C8)}
$$

and

$$
\mathbf{C} = \begin{bmatrix}
\mathbf{Z_{I5}} & \mathbf{Z_{R4}} & -\mathbf{Z_{I3}} & -\mathbf{Z_{R2}} & \mathbf{Z_{I1}}+\mathbf{M} & 0 & \mathbf{K} \\
-\mathbf{I} & 0 & 0 & 0 & 0 & 0 & 0 \\
0 & -\mathbf{I} & 0 & 0 & 0 & 0 & 0 \\
0 & 0 & -\mathbf{I} & 0 & 0 & 0 & 0 \\
0 & 0 & 0 & -\mathbf{I} & 0 & 0 & 0 \\
0 & 0 & 0 & 0 & -\mathbf{I} & 0 & 0 \\
0 & 0 & 0 & 0 & 0 & -\mathbf{I} & 0
\end{bmatrix}.
$$
$$\text{(C9)}$$

Berry, A. (**1990**). "A general formulation for the sound radiation from rectangular, baffled plates with arbitrary boundary conditions," J. Acoust. Soc. Am. **88**, 2792–2802.

Bowyer, E., and Krylov, V. V. (**2015**). "Experimental study of sound radiation by plates containing circular indentations of power-law profile," Appl. Acoust. **88**, 30–37.

Conlon, S. C., Fahnline, J. B., and Semperlotti, F. (**2015**). "Numerical analysis of the vibroacoustic properties of plates with embedded grids of acoustic black holes," J. Acoust. Soc. Am. **137**, 447–457.

Cunefare, K. A., and De Rosa, S. (**1999**). "An improved state-space method for coupled fluid-structure interaction analysis," J. Acoust. Soc. Am. **105**, 206–210.

Dana, M., Bernard, J., and Maxit, L. (**2020**). "A spectral global matrix method for modelling the response of a fluid-loaded multilayered cylindrical shell excited by an acoustic plane wave," J. Acoust. Soc. Am. **148**, 2997–3013.

Fahy, F., and Gardonio, P. (**2007**). *Sound and Structural Vibration* (Academic Press, New York).

Foin, O., Nicolas, J., and Atalla, N. (**1999**). "An efficient tool for predicting the structural acoustic and vibration response of sandwich plates in light or heavy fluid," Appl. Acoust. **57**, 213–242.

Giordano, J. A., and Koopmann, G. H. (**1995**). "State-space boundary element-finite element coupling for fluid-structure interaction analysis," J. Acoust. Soc. Am. **98**, 363–372.

Hambric, S. A., and Fahnline, J. B. (**2007**). "Structural acoustics tutorial—Part 2: Sound-structure interaction," Acoust. Today **3**, 9–27.

Krylov, V. V., and Winward, R. E. T. B. (**2007**). "Experimental investigation of the acoustic black hole effect for flexural waves in tapered plates," J. Sound Vib. **300**, 43–49.

Laulagnet, B., and Guyader, J. L. (**1989**). "Modal analysis of a shell's acoustic radiation in light and heavy fluids," J. Sound Vib. **131**, 397–415.

Li, S. (**2005**). "A state-space coupling method for fluid-structure interaction analysis of plates," J. Acoust. Soc. Am. **118**, 800–805.

Ma, L., and Cheng, L. (**2019**). "Sound radiation and transonic boundaries of a plate with an acoustic black hole," J. Acoust. Soc. Am. **145**, 164–172.

Ma, L., Zhang, S., and Cheng, L. (**2018**). "A 2D Daubechies wavelet model on the vibration of rectangular plates containing strip indentations with a parabolic thickness profile," J. Sound Vib. **429**, 130–146.

Mironov, M. A. (**1988**). "Propagation of a flexural wave in a plate whose thickness decreases smoothly to zero in a finite interval," Sov. Phys. Acoust. **34**, 318–319.

Nelisse, H., Beslin, O., and Nicolas, J. (**1998**). "A generalized approach for the acoustic radiation from a baffled or unbaffled plate with arbitrary boundary conditions, immersed in a light or heavy fluid," J. Sound Vib. **211**, 207–225.

O'Boy, D. J., and Krylov, V. V. (**2016**). "Vibration of a rectangular plate with a central power-law profiled groove by the Rayleigh–Ritz method," Appl. Acoust. **104**, 24–32.

Pelat, A., Gautier, F., Conlon, S. C., and Semperlotti, F. (**2020**). "The acoustic black hole: A review of theory and applications," J. Sound Vib. **476**, 115316.

Prill, O., and Busch, R. (**2016**). "Finite element simulations of acoustic black holes as lightweight damping treatments for automotive body panels with application to full vehicle interior wind noise predictions," in *INTER-NOISE and NOISE-CON Congress and Conference Proceedings* (Institute of Noise Control Engineering, Reston, VA), pp. 5210–5221.

Sandman, B. E. (**1975**). "Motion of a three-layered elastic–viscoelastic plate under fluid loading," J. Acoust. Soc. Am. **57**, 1097–1107.

Tabatabaian, M. (**2014**). *COMSOL for Engineers* (Mercury Learning and information, Dulles).

Tang, L., Cheng, L., Ji, H., and Qiu, J. (**2016**). "Characterization of acoustic black hole effect using a one-dimensional fully-coupled and wavelet-decomposed semi-analytical model," J. Sound Vib. **374**, 172–184.